Towards the continuous production of Pt-based heterogeneous catalysts using microfluidic systems

Laura Uson [a,b], Manuel Arruebo [a,b,*] and Victor Sebastian [a,b,*]

The continuous production of Pt-based heterogeneous catalysts based on ultra-small (< 2nm) noble metal nanoparticles deposited on mesoporous ordered silica and their catalytic activity in VOCs abatement are here reported. Microfluidic reactors can be used not only to enable the fast and controlled production of ultra small Pt nanoparticles (NPs), but also alloyed NPs including PtPd, PtRu and PtRh can be formed in short residence times (between 60 s and 5 min). A novel continuous and homogeneous loading of those catalytic NPs on SBA-15 used as mesoporous support is also here reported. This procedure eases the NPs loading and minimizes washing post-treatments. A 12-fold decrease in the synthesis time was obtained when using this microfluidic reactor compared to the traditional batch production of Pt NPs. Microflow and batch type reactors yielded a Pt precursor conversion to generate Pt NPs of 90% and 85%, respectively. Under the same conditions, the productivity of the microfluidic system (27 mg Pt NPs/h) was twice the one achieved in the conventional batch type reactor. The catalytic performance of the supported catalysts separately prepared by microfluidics and by conventional impregnation under the same conditions and with the same noble metal loading was also compared in the n-hexane abatement as a model of VOC. Both catalysts were active in the VOC oxidation reaction but a 95% reduction in the catalyst synthesis time was obtained when using the catalysts produced in the microfluidic platform. For this reaction a long-term activity test was successfully carried out at 175ºC during 30 h on stream using the heterogeneous catalyst prepared by using the flow reactor.

[a] *Department of Chemical & Environmental Engineering & Nanoscience Institute of Aragon (INA), University of Zaragoza, Mariano Esquillor edif. I+D, 50018 Zaragoza, Spain.*
[b] *CIBER de Bioingeniería, Biomateriales y Nanomedicina (CIBER-BBN), Centro de Investigación Biomédica en Red, C/Monforte de Lemos 3-5, Pabellón 11, 28029 Madrid, Spain*
[c] *† Footnotes relating to the title and/or authors should appear here.*
[d] *Electronic Supplementary Information (ESI) available: [details of any supplementary information available should be included here]. See DOI: 10.1039/x0xx00000x*

Introduction

The field of heterogeneous catalysis has received extraordinary efforts to rationalize the production of catalysts. Historically, the development of catalytic processes has been accomplished primarily by empirical trial and error processes[1]. Nowadays, a molecular driven approach is considered during the design of the catalyst in order to achieve molecular information of the catalytic reaction. The design of the supported catalysts is the most important aspect for improving and assuring their catalytic activity and selectivity along the time on stream. However, not only theoretical tools are required, but also better synthetic methods are needed to prepare catalysts that can fulfill the experimental conditions identified by such molecular studies[1].

Most heterogeneous catalysts are comprised of small nanoparticles (NPs) of an active phase finely dispersed on a high-surface-area support to maximize the surface-to-volume ratio of this active phase. A number of chemical methods based on wet-chemistry have been developed for the synthesis of platinum NPs, exhibiting a fine control in size and shape[2-4]. But some of these procedures render nanoparticles with a low yield[5]. Unfortunately, some reported methods applied during catalyst production render NPs with a wide range of sizes and shapes[5-9], hampering their direct use until purification methodologies were applied[10]. In addition, the scaled-up production is limited due to the inherent limitations of conventional batch type reactors, such as heat and mass transfer constraints.[11] These facts mean that following those traditional methods the resulting catalysts show no molecular control on their active sites[1, 3, 12-15]. Then, controlling the size and shape of the supported nanoparticles used as catalysts can involve profound changes in the catalytic behavior by exposing a large amount of catalytically active crystal facets or edges to the reacting fluids [16-18].

The preparation of high-surface-area catalysts with size-controlled NPs is usually carried out by depositing pre-prepared metal colloids on a given support by any of the following approaches: adsorption of the metal-based colloids, grafting on the support, flame spraying techniques, the Langumir-Blodgett technique, etc.[19]. However, the challenge in the preparation of high-surface-area heterogeneous catalysts is to disperse the colloidal NPs in the entire surface area without losing the original nanoparticle-size distribution [1].

In our previous work[20] we described a new method to obtain < 2 nm wide variety of noble metal (Pt, Ru, Pd) and alloyed bimetallic and trimetallic nanocrystals. The reported procedure rendered < 2 nm nanoparticles with an excellent control in the size distribution and chemical composition. The use of the organophosphorus salt tetrakis-(hydroxymethyl)-phosphonium chloride (THPC) and its double role as stabilizing and reducing ligand, enabled an easy and versatile procedure to generate different type of noble-metal nanocrystals in conventional laboratory-scale batch reactors with 15 mL (1 mM) production scale. Afterwards, the synthesis procedure of noble metal NPs based on the double role of THPC has been successfully adopted in the production of various types of catalysts[21-28].

Although the previously reported results using THPC[20, 29] were well adopted and were very promising to produce a variety of stable noble metal NPs with an exquisite size control, there are several issues that still should be improved: a) The production throughput is limited due to the long synthesis-time required (i.e., 96h); b) A reproducible, efficient and easily scalable procedure should be designed; c) NPs should be homogeneously supported in order to be applied in any heterogeneous catalytic reaction.

Continuous flow technologies offer potential advantages over batch synthesis, including feedback control over temperature and flow rates, reproducibility, potential for sensor integration and a consequent *in situ* synthesis monitoring, rapid screening of parameters, safety, and easy scale-up [30, 31]. The large surface to volume ratio of microfluidic reactors (MR) and the limited diffusion paths in microchannels, enhance heat and mass transfers.[32] These facts arise the ability to work at elevated temperatures and pressures, as well as in accelerating nanoparticle production. For instance, it is well-stablished that the microfluidic continuous synthesis at elevated temperatures and pressures produces nanostructures on the time scales of seconds to minutes, in contrast to the time scale of hours reported in traditional batch procedures [33-38]. These overwhelming improvements were achieved by modifying the reactor and the synthesis conditions: temperature, pressure, reactants, residence time and flow conditions[34, 39].

One reason for selecting a continuous operation approach in catalyst production is that the yearly production rates of catalysts can be rather small, comparable to pharmaceutical or fine chemical syntheses [40]. With the advent of microfluidic systems, the small-scale preparation of products in a continuous operation mode is very attractive. In addition, the preparation of catalysts in a continuously operated flow system is still a research field with only a few published results [41]. Being most of the works focused on the precipitation of hydroxides, oxides or other hardly soluble metal compounds [42].

Most volatile organic compounds (VOCs) can be responsible for long-term harmful health effects and are considered as one of the major contributors to air pollution [24, 43]. The best alternative to control VOCs pollutants is eliminating them prior to the discharge. Among the different technologies that have been arisen to face VOCs pollution, low-temperature (20–400 ºC) catalytic oxidation has been evidenced as one of the most reliable and effective post-treatment technologies [43]. Due to their outstanding catalytic performance, noble metal-based catalysts are widely used in VOCs decomposition, exhibiting higher low-temperature activity than those obtained with metal oxides. Among those noble metal catalysts, Pt-based catalysts usually render the most significant low-temperature activity in VOCs oxidation [43.] Several methods have been reported for producing noble-metal NPs supported on high-surface area materials, but, to the best of our knowledge, this work describes a new approach to produce Pt-based heterogeneous catalysts (i.e., Pt-based NPs supported on mesoporous silica) in a continuous manner with an exquisite control of the active phase, dimensions and loading process (Figure 1). Ultra-small NPs were produced in continuous flow under the timeline of 90 s using a fast and potentially easily scalable procedure by a numbering-up approach. The produced nanoparticles were afterwards homogenously loaded in a functionalized mesoporous material in order to provide with the ease of manipulation during catalysis. Finally, an activity test for the resulting mesoporous catalysts was determined in hexane abatement, used as a model of a typical VOC (Figure 1).

Experimental Section

Reactants

NH_4F (98%, ACS reagent, Fluka), Pluronic P123 (Sigma), Tetraethylorthosilicate (TEOS, 98%, Sigma), Heptane (99%, Reagent Plus, Sigma), triethoxysilane (APTES, 98%, Sigma), Chloroplatinic acid solution (H_2PtCl_6, 8wt.%, Sigma), Tetrakis (hydroxymethyl)phosphonium chloride solution (THPC, 80% in H_2O, Sigma), potassium tetrachloropalladate (II) (K_2PdClO_4, Sigma), Ruthenium (III) Chloride ($RuCl_3$, Sigma), Rhodium (III) chloride hydrate ($RhCl_3$, Sigma), and 3-(trimethylsilyl)propionic-2,2,3,3-d4 acid sodium salt (TSP, Aldrich) were used.

Microfluidic system description

Synthesis of metal nanoparticles

Figure 2 shows the experimental microfluidic platform used in this work to synthesize the metal NPs used as catalysts. Two reagent streams, Q1 and Q2, were injected in the continuous flow system described using syringe pumps (Harvard apparatus PHD ULTRATM CP 4400). Q1 consisted of a mixture of NaOH (20 mM) and H_2PtCl_6 (2.5 mM), and Q2 was composed of a 3 mM solution of THPC (Figure 2-a). Figure 2-b depicts the microfluidic system composed of two stages: 1) a micromixing stage maintained at room temperature to promote reagents mixing before the nanocrystallization stage and 2) a reaction stage using a PTFE tubing loop located in a thermostatic bath to tune the nanocrystallization kinetics. A micromixer chip (Dolomite, internal volume = 8 μL) was selected for the micromixing stage to achieve a fast mixing (Figure 2-b). The reaction PTFE loop was assembled with a microtubing (I.D. =

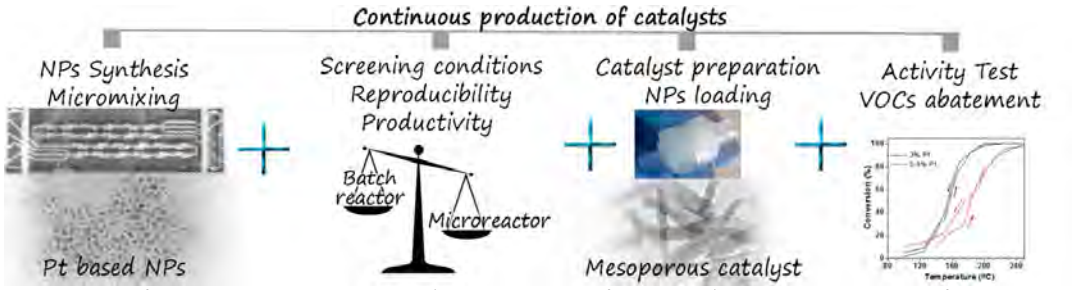

Figure 1.- .- Scheme of the main stages developed in this work: 1) NPs synthesis in a microfluidic system; 2) Screening conditions and study of reproducibility and productivity; 3) Catalyst loading in microfilters using mesoporous silica as support and 4) Activity test in VOCs abatement reaction.

793 µm, volume of 2.8 mL and a length of 1.9 m[u1]). Reaction temperature and residence time were varied in the reaction stage to study the best synthesis conditions in the production of metal NPs in a continuous fashion. The total concentration of noble metal reagents in the production of Pt-M alloyed nanoparticles was similar to the one used in the pure Pt NP synthesis (2.5mM), but the molar ratio Pt/M was maintained as 1, being M= Rh, Ru and Pd)

The synthesis of metal NPs at high temperature in a batch type reaction was adapted from a previous described procedure. [20] Pt nanoparticles were produced at 95ºC using the organophosphorous salt THPC as simultaneous reducing and stabilizing agent. In a typical synthesis, 100 µL of H_2PtCl_6 and 167 µL of NaOH 1M were dispersed in 15 mL of double deionized (DDI) water. The solution was heated in an oil bath at 95ºC in a 2.6 cm diameter glass vial. 333 µL of a 65 mM THPC solution were added to the heated vial and left under stirring for the estimated time.

The NP production yield was calculated by plasma atomic emission spectroscopy (MP-AES) after separating metal cations from metal NPs by a dialysis membrane (D9652 Sigma-Aldrich). Both, the dialysis membrane retentate and the dialyzed solution were analyzed. The yield was averaged by using 2 samples of Pt NPs, obtaining a standard deviation of 4.3% for the batch synthesis and 3.7% for the continuous synthesis.

Synthesis of SBA-15 nanorods as supports

SBA-15 nanorods (SBA-15 NRs) were synthesized following the protocol described by Johansson et al.[44] In brief, 1.2 g of Pluronic P123 and 0.014 g of NH_4F were dissolved at 20ºC in 40 mL of HCl (1.75M) under stirring. 9.5 mL of heptane were premixed with 2.75 mL of TEOS and added to the first solution once the Pluronic P123 was totally dissolved. The resulting solution was kept under vigorous stirring for 4 min and then under static conditions for 8 min. Afterwards, the mixture was hydrothermally heated at 100ºC for 24h in a Teflon lined autoclave. Then, the collected solid product was filtered and washed with distilled water. Finally, the material was calcined in a furnace with a heating ramp of 0.5ºC/min up to 550ºC and a dwell time of 5 hours at 550ºC. The resulting rods were post-grafted with amine terminal groups to facilitate noble metal attachment with the aid of (3-Aminopropyl)triethoxysilane (APTES, ≥ 98% Sigma-Aldrich) following a previously described experimental protocol [45].

Pt NPs loading in mesoporous SBA-15 NRs

A dispersion of APTES functionalized SBA-15 NRs (10 mg/mL) were sonicated and injected with a flow rate of 1 ml/min into a commercial filter holder (Swinnex-13, Millipore) containing a cellulose filter to generate a mesoporous SBA-15-based filter cake. The thickness of the filter cake could be tuned according to the mass of APTES-SBA-15 NRs injected. A colloid with the proper concentration of Pt NPs was injected (i.e., 0.5 mL/min if one filter holder was used) into the commercial filter holder to promote the loading of the noble metal into the SBA-15 mesopores. Finally, the resulting supported catalyst was flushed with distilled water to remove any NP weakly anchored to the mesoporous matrix.

Activity test: oxidation of n-hexane.

The catalytic activity of the Pt-APTES SBA-15 NRs catalysts (3 wt.% Pt) was tested in the reaction of oxidation of n-hexane. The catalyst (30 mg) was introduced in a quartz fixed-bed reactor and it was packed with the aid of glass wool. The total gas flow rate was adjusted to reach a reactant gas flow rate/reactor volume (GHSV) of 31.000 h^{-1}. The concentration of n-hexane used was 200ppm. The catalyst pre-treatment included two oxidation cycles at 250ºC under air flux and one reductive cycle at the same temperature under N_2/H_2 (volume ratio 71.5/28.5). The reaction temperature was measured by a

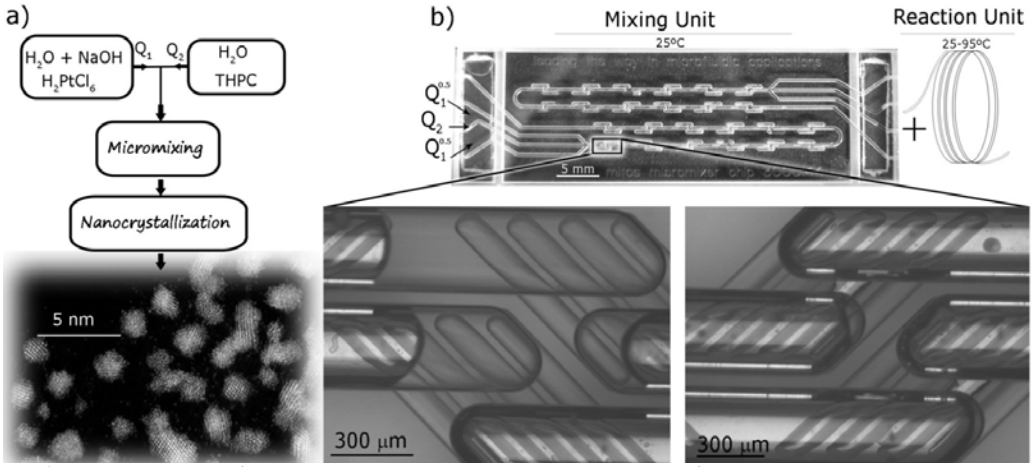

Figure 2. a) Schematic representation of the synthesis procedure to produce noble metal NPs in continuous flow, using THPC as a reducing and stabilizing agent. b) Microfluidic system to produce noble metal NPs: Micromixing unit (Inset: high magnification of a micromixing stage) and reaction unit.

mobile thermocouple located at the surface of the catalyst in the gas exhaust side. The catalyst was tested from 25ºC up to 250ºC, with temperature increments of 25ºC. Reaction temperatures were stabilized for 60 min to ensure a stable conversion determination.

The gases were analyzed by online gas chromatography (Agilent 3000 Micro GC) which under our experimental conditions gave an n-hexane detection limit of 3 ppm. Maximum error in the balance closures for carbon and oxygen was ± 2%. n-hexane conversion values were calculated according to Eq 1, where $F_{n\text{-hexane}}$ is the molar flow rate of n-hexane at the inlet or outlet of the catalytic test reactor

Eq. 1. $$n-hexane\ conversion\ (\%) = \frac{F^{inlet}_{n-hexane} - F^{outlet}_{n-hexane}}{F^{inle\ t}_{n-hexane}}$$

Electron Microscopy characterization.

Preliminary electron microscopy observations were carried out using a T20-FEI microscope with a LaB6 electron source fitted with a "SuperTwin®" objective lens allowing a point-to-point resolution of 2.4 Å. Aberration corrected scanning transmission electron microscopy (Cs-corrected STEM) images were acquired using a high angle annular dark field detector in a FEI XFEG TITAN electron microscope operated at 300 kV equipped with a CETCOR Cs-probe corrector from CEOS. Elemental analysis was carried out with an EDS (EDAX) detector, which allows performing EDS experiments in the scanning mode. Scanning Electron Microscopy images were obtained using an Inspect F-50 SEM microscope. Metallic elemental analyses by EDS (energy dispersive spectroscopy) were carried out with an INCA PentaFET x3 (Oxford Instruments). The amount of Pt incorporated onto the SBA-15 catalyst was determined by using a microwave plasma-atomic emission spectrometer (Agilent 4100 MP-AES) after sample digestion with a mixture of HNO_3/HCl (1:3 v/v). The specific surface area and pore volume distribution were measured by nitrogen adsorption at 77K in a Micromeritics ASAP2020. SBA-15 NRs were out-gassed at 26.7 Pa and 473 K for 8h before the measurement. APTES SBA-15 NRs were out-gassed at 26.7 Pa and 383 K for 10 h to prevent damage of the organic groups.

Results and discussion

Synthesis of Pt-based colloids in continuous flow

Fast nanocrystallization reactions carried out under a good control of size, shape and composition require that the mixing time must be considerably smaller than the reaction time [46]. Then, the presence of a micromixing unit is critical in controlling the formation of NPs in continuous flow reactors, especially during fast kinetic reactions [46, 47]. Figure 2 illustrates the microfluidic system utilized in this work to synthesize Pt based NPs. Mixing and reaction stages are separated to gain control during the NPs growth. The mixing unit is constituted by a glass micromixer that it is structured in 12 micromixing stages that render the lamination of the flow streams, reduce the diffusion distances and hence, reduce the mixing time (Figure 2-b). Reagents were introduced in two separated

streams, Q1 and Q2, to prevent THPC activation by hydroxide anions and to better control the reaction kinetics (Figure 2-a). THPC hydrolysis produces formaldehyde, which requires the presence of OH^- ions to enhance the formaldehyde oxidation reaction (Eq. 2). Then, formaldehyde acts as reducing agent of metal ions. This fact implies that the metal NPs cannot be produced if the concentration of OH^- ions were not the proper one [20].

Eq. 2 $HCHO+H_2O \rightarrow 4H^+ + CO_2\,(g)+ 4\,e^-$

Residence time and synthesis temperatures at the reaction stage were tuned in order to produce monodispersed Pt NPs with high throughput. Reaction temperatures were varied between room temperature and 95ºC at a constant residence time (11 min).

The formation of Pt NPs could be easily tracked by the color of the formed colloid, obtaining a black color when Pt NPs were produced. Under the tested conditions, Pt NPs were only formed when the reaction temperature was higher than 80ºC (Fig. 3-a). It can be inferred from these results that as it was expected, high temperature increases the reduction rates during the nucleation and growth stages of NPs formation. A higher reduction rate during the nucleation stage will result in a high population of nuclei and smaller Pt NPs. However, a high temperature during the growth stage can also promote the coalescence of crystallites, rendering a heterogeneous Pt nanoparticle-size distribution [48]. Then, a balance is required to fine control the NP growth. In addition, this microfluidic system was operating under autogenous pressure and it is important to point out that a temperature higher than 95ºC would create flow instability due to the flashing evaporation of water.

The residence time was varied from 3 minutes to 60 s at a reaction temperature of 95ºC. Considering that the volume of the reaction unit was kept constant, the residence time was tuned by the variation of the reagent flow rates. The formation of Pt NPs was only produced at a residence time larger than 90 s (Figure 3-b). It was observed that the color of the dispersion collected at a residence time of 60 s evolved after several minutes from transparent to black color. This insight obviously implies that the growth stage in the crystallization process was not sufficiently promoted after 60 s of residence time. Consequently, the optimum synthesis conditions to achieve a fast production of Pt NPs were set at 95ºC, 90 s and a total flow rate of 1.9 mL/min. Figure 3-d shows a TEM image of the as-made Pt NPs, rendering a particle-size distribution of 1.9±0.3 nm and a dispersity (d) of 0.15 (dispersity= Standard deviation/mean value). Ultra-high resolution STEM shows that the NPs produced in a residence time as short as 90 s have a reduced dispersity and are highly crystalline, evidencing the excellent crystallization control achieved in the proposed multi-stage microfluidic system (Figure 3-d). The Pt NPs produced by this fast continuous approach presented the same specifications that the ones produced in batch conditions by the reported procedure at room temperature and 96 h of reaction (Figure 3 f-g) [20]. The mixing stage was modified using a Y junction as a micromixer. The mixing in the Y junction is not as good as the one achieved in the 3-D micromixer depicted in

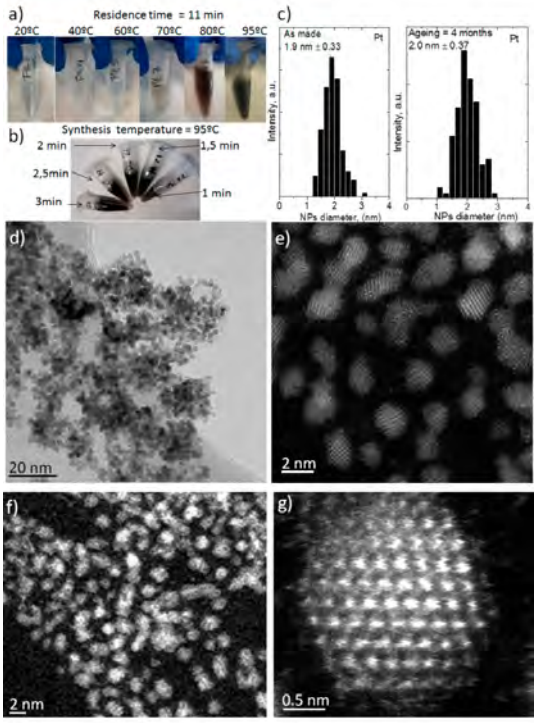

Figure 3. a) Optical image of the Pt colloid collected in the microfluidic system at different synthesis temperatures (reaction unit) with a constant residence time = 11 min. b) Optical image of the Pt colloid collected in the microfluidic system at different residence times with a constant synthesis temperature = 95ºC. c) Particle-size distribution histograms measured by TEM from as-made and aged for 4 months Pt NPs (at least 300 particles were measured per sample). [49] d) TEM image of Pt NPs produced at 95ºC with a residence time = 1.5 min. e) Ultra high resolution STEM-HAADF image of Pt NPs depicted in d) where atomic columns are clearly observed. Pt NPs produced in a batch type reactor at 25ºC and a synthesis time of 96h: f) STEM-HAADF images of the Pt NPs colloid, g) UHR-STEM-HAADF image of a Pt NP.

Figure 2 and Pt NPs were not properly obtained at the same synthesis conditions. This fact is a clear evidence of the need of having a good mixing to activate the THPC to generate the reductant species.

A batch type reactor was selected to benchmark the synthesis conditions optimized by the microfluidic reactor approach at 95ºC. The formation of Pt NPs in a batch type reactor was observed to proceed after a synthesis time of 18 minutes. It implies that the microfluidic reactor system accelerates the nucleation stage and then, microflows enable to achieve the same quality of Pt NPs than the ones produced in batch type reactors, [20] but with a considerable time savings (12 fold). The synthesis yields achieved in both syntheses were estimated by Microwave Plasma-Atomic Emission Spectrometry analysis (MP-AES). Microflow and batch type reactors yielded a Pt^{2+} conversion to Pt NPs of 90% and 85%, respectively. The productivity of the microfluidic system (27 mg Pt NP/h) is two-fold larger than the one achieved in the batch type reactor at 95ºC (13 mg Pt NP/h, considering the reactor volume reported[20]). As a consequence of the higher productivity of the continuous approach and the easy

scalability of the reaction conditions by numbering-up the amount of microreactor units, we envisage that the proposed production system is a versatile system towards the continuous production of ultra-small metal nanoparticles.

The reproducibility of the continuous synthesis procedure was tested at least 10 times to confirm that the microfluidic system is a robust tool to face the lack of reproducibility in nanomaterials production when using batch reactors. According to the microscopy images and colloid hue (Figure S1), the microfluidic system demonstrated good run-to-run reproducibility.

The fast production of Pt NPs in the microfluidic system can be argued by the fast supersaturation of Pt atoms achieved during the nucleation stage. The surface to volume ratio of the considered microfluidic and batch type reactors were 2515 and 189 m^2/m^3, respectively. Considering that the heat transfer is proportional to the surface exchanged area, it can be concluded that the heat flow rate in the microfluidic system overpasses the one achieved in the batch reactor by one order of magnitude. Then, the fast heat transfer enables a fast nucleation of metal atoms and the subsequent NPs growth.

On the other hand, the continuous produced Pt NPs were aged at room temperature for 4 months to study if they were unstable, obtaining that the particle-size distribution was similar to the one retrieved from the as-made NPs (Figure 3-c). This fact supports again the quality and growth control achieved in the fast microfluidic production of Pt NPs.

Pt nanoalloyed colloids were also produced to demonstrate the chemical versatility of the proposed microfluidic system. Pd, Ru and Rh metallic precursors were injected together with the Pt precursor through the Q1 flow inlet. The same optimization criteria applied in the continuous production of Pt NPs were followed to obtain PtPd, PtRu and PtRh alloyed NPs (Figure 4). However, the residence time required to produce homogenous and stable NPs at 95ºC varied according to the noble metal selected. PtPd NPs could be produced in a residence time of only 60 s, but PtRu and PtRh required increasing the residence time up to 4 and 5 minutes, respectively. A feasible reason to understand the different nanocrystallization performance observed between Pt and PtPd, as well as PtRu and PtRh alloyed NPs could be attributed to their different reduction potentials. Pt and Pd have the highest reduction potentials, and therefore they should be reduced to metal atoms faster than Ru and Rh (Figure 4-a). Figure 4-b-d depicts the STEM-HAADF images and EDX spectra of PtRh, PtRu and PtPd NPs to demonstrate that the metals were localized in the same NP. The particle-size distribution of each type of NP was similar to the one measured for Pt NPs. However, PtPd NPs (d=0.25) and PtRu (d=0.21) were relatively monodisperse in comparison with PtRh (d= 0.13) (Figure 4). High-angle annular dark field (HAADF) detector shows atomic number contrast for high scattering angles of the electrons. The lack of z-contrast in STEM-HAADF images and EDX analysis confirmed the formation of alloyed NPs instead of segregated ones (Figure 4). Concluding that the reported procedure not only enabled the fast and controlled production of Pt NPs, but also the formation of alloyed NPs.

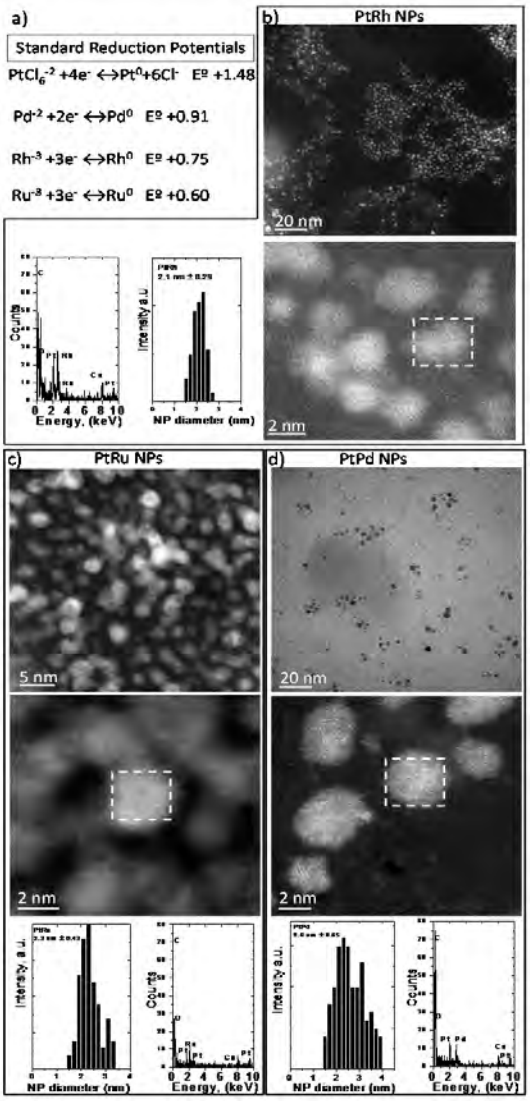

Figure 4.a) Standard reduction potentials of metal ions used in the formation of Pt based nanoalloys. STEM HAADF and HRSTEM-HAADF images, particle-size distribution histograms measured by TEM (at least 300 particles were measured per sample[49]) and EDX spectra from the area marked with a white striped square: b) PtRh NPs, c) PtRu NPs and d) PtPd NPs.

Pt-mesoporous catalyst production

As it was aforementioned, SBA-15 mesoporous nanorods (SBA-15 NRs) were synthesized following the protocol described by Johansson et al. [44]. The resulting nanorods were

~500 nm long and had a diameter of 150 nm Figure 6-d). The calculated BET surface area of 650 $m^2 \cdot g^{-1}$ was in agreement with the reported data [44].

Nanorods were functionalized with amine groups as electron donors to anchor the noble NPs to the mesoporous support (APTES-SBA-15 NRs). The calculated BET surface area decreased to ca. 350 $m^2 \cdot g^{-1}$ after the amination step due to the amino grafting on the pore-wall surface. Commercial filter holders were selected to generate a mesoporous filter cake that could be loaded with Pt NPs in a continuous flow (Figure 5-a,b). The thickness of the mesoporous cake was tuned according to the mass of APTES-SBA-15 NRs injected, obtaining a good and reproducible loading control (Figure 5-c). As-made Pt NPs produced by the continuous approach were injected into the filter holder to promote the diffusion of the Pt NPs through the mesoporosity of each nanorod (Figure 5-d). It must be noticed that the accessibility of Pt NPs to the interparticle surface of APTES-SBA-15 NRs is higher than that observed for the intra-mesoporous channels due to the reduced pressure drop. However, the external surface area of SBA-15 nanorods is less than 0.5 % of the accessible surface area [50]. In addition, after Pt loading, distilled water was injected to the filter holder to minimize the formation of aggregates of Pt NPs on the interparticle area of APTES-SBA-15 NRs and to reduce the potential leftover Cl^- ions which could produce catalyst deactivation.

The parallelization of Pt loading to increase the productivity of the Pt-loaded mesoporous catalysts was considered. The distribution of Pt streams through the mesoporous support was a crucial parameter to obtain a homogenous Pt loading through each mesoporous cake. Figure S2 depicts a comparison between the Pt-loaded mesoporous cakes produced with different flow splitters. The Pt loading in the mesoporous substrate could be evidenced by the change in the color from white to black (Figure 5-e). Then, a visual macroscopic inspection of the Pt-cakes obtained after

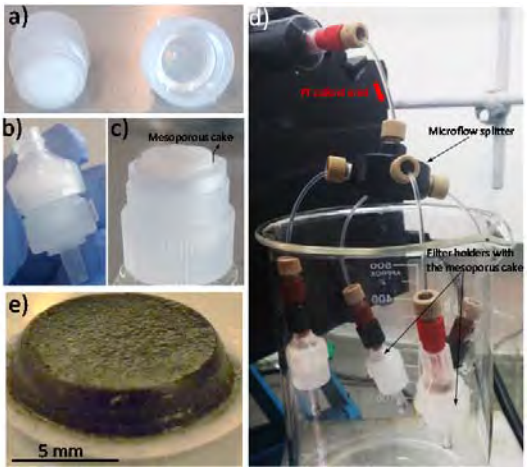

Figure 5.- a-b) Optical images of the selected filter holder to carry out the mesoporous cake formation and Pt NPs loading. c) Optical image of the mesoporous cake formed. d) Optical image of the set-up designed with a 4-fold flow splitter to produce Pt-loaded mesoporous cakes. It can be observed the four-fold flow splitting that enables a homogenous distribution of the Pt colloid through the filter holders. e) Pt-loaded mesoporous cake after the washing treatment.

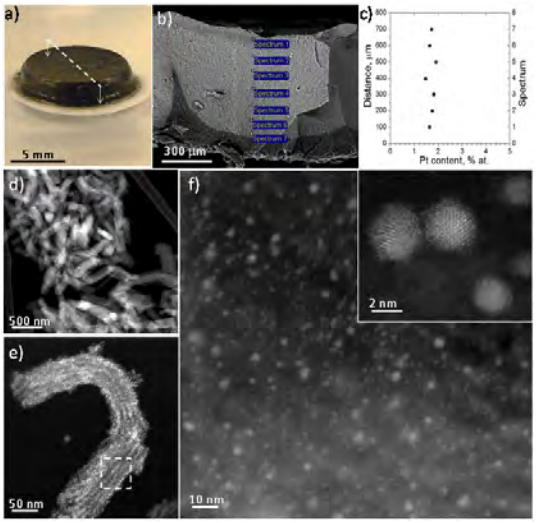

Figure 6.- a) Optical image of a Pt-loaded mesoporous cake, the cross-section was analysed to determine the Pt content profile. b) SEM image of the cross-section of a mesoporous cake. c) Pt content quantified by EDS analysis at the locations marked in b). d) STEM–HAADF image of the produced Pt-APTES-SBA-15 NRs, e) STEM-HAADF image of a Pt loaded APTES-SBA-15 NR. Mesoporous channels can be observed. f) STEM-HAADF image with high magnification of the area marked in e) showing the Pt NPs distribution on a APTES-SBA-15 NR. Inset depicts Pt nanocrystals with high crystallinity.

washing, showed if a homogenous distribution of the Pt colloid were produced. Undoubtedly, the best results were achieved when using a four-fold flow splitter (Figure 5-c,e), where the Pt loading could be adjusted by modifying the Pt NP concentration of the colloid injected. Figure 6-b depicts a SEM image of the cross-section of one of the Pt-loaded cakes produced with a four-fold flow splitter. The lack of cavities in the cake and the high grade of compactness observed drew the conclusion that the proposed method enabled to achieve a homogenous cake where the fluid could diffuse without channeling or without the presence of bald spots. The high mesoporosity of the SBA-15 (9.6 nm) together with a reduced interparticle porosity (i.e., estimated with the same size than the nanorods, 500x150 nm) and overpressure pump injection favoured the colloidal Pt to diffuse throughout the inner silica mesopores. To ratify this assumption, an energy-dispersive X-ray spectroscopy (EDS) profile was conducted along the cross-section of the Pt-loaded mesoporous cakes. This EDS analysis evidenced that a homogenous loading of Pt was achieved since the concentration of Pt was similar at all analyzed locations (Figure 6-c). It must be highlighted that this achievement is outstanding because if the distribution of APTES-SBA-15 NRs and Pt colloid were not homogenous, a heterogeneous Pt loading would have been generated. In fact, this phenomenon was observed when other flow distributors were selected rather that the four-fold flow splitting (Figure S2). Finally, Figure 6 e-f and Figure S3 show STEM-HAADF images of a Pt-loaded APTES-SBA-15 NR. It can be observed that the Pt NPs (bright contrast dots) are homogenously distributed along the nanorod. Then, it can be inferred from this result that the flow distribution was properly managed to enable the Pt colloid to

diffuse not only between the nanorod interporosity but also inside the mesoporous channels to offer excellent catalysis dispersion.

One of the advantages of the method here described is that the catalyst can be easy washed out to eliminate any Pt NPs that were not anchored to the mesoporous support, just by injecting distilled water through the filter holders. It must be highlighted that the washing post-treatment of catalysts is a time consuming operation, but it is crucial during catalyst preparation to reduce the content of ions that could inhibit the catalyst performance [51].

Pt-mesoporous catalyst activity test: oxidation of n-hexane

It is well known that noble metal loading and dispersion are two principal factors influencing the catalytic capability. According to aforementioned results, it is clear that the proposed methodology enables to obtain a good control on the Pt NPs dispersion. Pt loading in APTES-SBA-15 NRs was tuned by adjusting the concentration of Pt NPs during their injection through the filter holders. Two catalysts with a Pt loading of 0.9 and 3 wt.%, respectively were prepared and tested in n-hexane abatement. Figure 7-a shows the catalytic performance of the prepared catalysts as a function of the reaction temperature. As expected, VOC conversion increased with an increase in the reaction temperature, achieving a 100% n-hexane removal efficiency. However, the higher density of active sites presented in the catalyst with 3 wt.% Pt loading resulted in a reduction of 40 ºC in the light-off temperature (Pt 3% T_{50}= 150ºC, Pt 0.9% T_{50}=190ºC) and in 50ºC for the total n-hexane conversion (Pt 3% T_{100}= 200ºC, Pt 0.9% T_{100}=250ºC). The catalytic performance observed in the tested catalysts was similar during the heating and cooling cycles (Figure 7-a). This finding reveals that the catalysts produced did not deactivate during the process of oxidation. According to the most accepted mechanism of catalytic oxidation (Langmuir–Hinshelwood and Eley–Rideal), noble metals are believed to function at their reduced states[52], and then, catalysts sensitive to the oxidation state could deactivate.

Figure 7-b depicts the catalytic performance of the 3 wt.% Pt catalyst prepared according to: i) conventional methodology in a magnetically stirred reactor by impregnation following a washing treatment made by centrifugation and ii) in the microfluidic system reported in this work. Both catalysts were active for the VOC oxidation reaction, exhibiting a similar trend and removal efficiency. Although both considered methodologies render the same activity for n-hexane abatement, it should be highlighted that the time savings in the catalyst preparation (loading and washing) using microfluidics was reduced over 95%, as well as the aforementioned cited advantages. Finally, it is reported that the noble metal catalysts in VOCs oxidation reaction are easily deactivated by the formation of coke, chlorinated oxide or water on their surfaces [43]. Then, a long-term activity test was carried out at 175ºC during 30 h, without observing any signs of catalytic deactivation (Figure 7-c). Figure S2 presents a STEM-HAADF image of the catalyst after 30 h on stream. It can

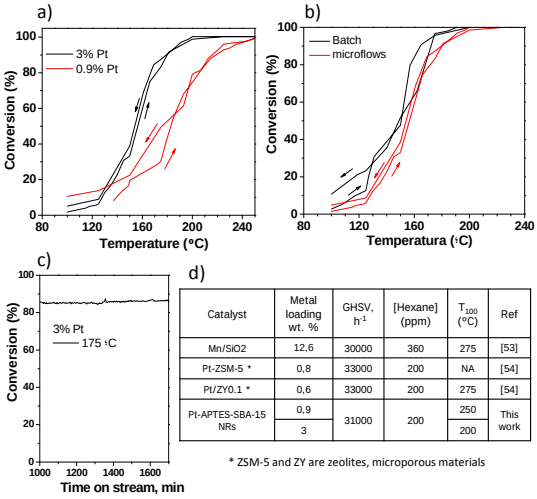

Catalyst	Metal loading wt. %	GHSV, h^{-1}	[Hexane] (ppm)	T_{100} (ºC)	Ref
Mn/SiO2	12,6	30000	360	275	[53]
Pt-ZSM-5 *	0,8	33000	200	NA	[54]
Pt/ZY0.1 *	0,6	33000	200	275	[54]
Pt-APTES-SBA-15 NRs	0,9	31000	200	250	This work
	3			200	

* ZSM-5 and ZY are zeolites, microporous materials

Figure 6.- a) Catalytic performance of Pt-APTES-SBA-15 NRs with a Pt loading of 0.9 and 3 wt.%. b) Comparison between catalyst prepared by microfluidics and conventional procedures. c) Conversion as a function of time on stream at a fixed temperature of 175 ◦C; measurements were performed with a GHSV = 31000 h^{-1} under a hexane concentration of 200 ppm. d) Previous literature data for catalytic n-hexane combustion.

be observed the absence of Pt agglomerates or aggregates potentially formed by coalescence or sintering.

Figure 7-d summarizes the total combustion temperature for n-hexane abatement with different catalysts retrieved from the literature at similar reaction conditions than the ones used in this work. The temperature obtained in this work for 100 % removal efficiency over performs the reported activity results with a comparative Pt loading [53, 54]. This performance can be attributed to the small dimensions of Pt NPs and high dispersion achieved in the mesoporous structure of the SBA-15 NRs.

Conclusions

Commercially available micromixers can be easily interfaced with polymeric tubing to create a multistage which allows a controlled separation of nucleation and growth of metal noble NPs as well as their alloys. Depending on the standard reduction potentials of the noble metals used as precursors the microfluidic platform can be easily used to produce Pt NPs but also PtRh, PtRu and PtPd by varying the residence times between 60 s and 5 minutes. The colloidal ultrasmall NPs were deposited on amino-functionalized SBA_15-based mesoporous cakes in a continuous manner and also using flow distributors. This novel procedure allows multiple parallelizations and minimizes the time consuming operation of washing post-treatment. In a comparative batch reactor the production of Pt nanoparticles took up to 18 min whereas double production was achieved in the microfluidic reactor in only 90 s under the same synthesis conditions. The catalytic oxidation of n-hexane (200 ppm) was evaluated for the heterogeneous catalyst here described showing a total n-

hexane removal with light-off temperatures as low as 200ºC. For this catalyst, a long-term activity test was carried out at 175ºC during 30 h, without observing any signs of catalytic deactivation.

Acknowledgements

Financial support from the EU thanks to the ERC Consolidator Grant (ERC-2013-CoG-614715, NANOHEDONISM) and People Program (CIG-Marie Curie Actions, REA grant agreement no. 321642) are gratefully acknowledged. CIBER-BBN is an initiative funded by the VI National R&D&i Plan 2008–2011, Iniciativa Ingenio 2010, Consolider Program, CIBER Actions and financed by the Instituto de Salud Carlos III (Spain) with assistance from the European Regional Development Fund

Notes and references

1. F. Zaera, *Catal Lett*, 2012, **142**, 501-516.
2. J. Chen, Y. Xiang, Y. Yin and Y. N. Xia, *Small*, 2006, **2**, 1399-1399.
3. R. Narayanan and M. A. El-Sayed, *Nano Lett*, 2004, **4**, 1343-1348.
4. X. W. Teng and H. Yang, *Nano Lett*, 2005, **5**, 885-891.
5. S. Kundu and H. Liang, *Langmuir*, 2010, **26**, 6720-6727.
6. J. Yang, J. Y. Lee and H. P. Too, *Anal Chim Acta*, 2005, **546**, 133-138.
7. T. Teranishi, R. Kurita and M. Miyake, *J Inorg Organomet P*, 2000, **10**, 145-156.
8. J. M. Petroski, Z. L. Wang, T. C. Green and M. A. El-Sayed, *J Phys Chem B*, 1998, **102**, 3316-3320.
9. M. N. Mankin, V. Mazumder and S. H. Sun, *Chem Mater*, 2011, **23**, 132-136.
10. T. P. Tyler, A. I. Henry, R. P. Van Duyne and M. C. Hersam, *J Phys Chem Lett*, 2011, **2**, 218-222.
11. V. Sebastian, M. Arruebo and J. Santamaria, *Small*, 2014, **10**, 835-853.
12. G. A. Somorjai and J. Y. Park, *Top Catal*, 2008, **49**, 126-135.
13. S. E. Habas, H. Lee, V. Radmilovic, G. A. Somorjai and P. Yang, *Nat Mater*, 2007, **6**, 692.
14. H. Lee, S. E. Habas, S. Kweskin, D. Butcher, G. A. Somorjai and P. Yang, *Angew. Chem. Int. Ed.*, 2006, **118**, 7988-7992.
15. K. M. Bratlie, H. Lee, K. Komvopoulos, P. Yang and G. A. Somorjai, *Nano Lett*, 2007, **7**, 3097-3101.
16. V. Sebastian, S. Basak and K. F. Jensen, *Aiche J*, 2016, **62**, 373-380.
17. A. Lopez, A. Larrea, V. Sebastian, M. P. Calatayud, S. Irusta and J. Santamaria, *Chemcatchem*, 2016, **8**, 1479-1484.
18. G. J. Hutchings and M. Haruta, *Appl Catal a-Gen*, 2005, **291**, 2-5.
19. C. J. Jia and F. Schuth, *Phys Chem Chem Phys*, 2011, **13**, 2457-2487.
20. J. L. Hueso, V. Sebastian, A. Mayoral, L. Uson, M. Arruebo and J. Santamaria, *RSC Adv*, 2013, **3**, 10427-10433.
21. A. Ramirez, V. Sebastian, R. Mallada, J. Santamaria and A. Monzon, *Appl Catal a-Gen*, 2015, **505**, 193-199.
22. A. Eguizabal, L. Uson, V. Sebastian, J. L. Hueso and M. P. Pina, *Rsc Adv*, 2015, **5**, 90691-90697.
23. L. Gomez, J. L. Hueso, M. C. Ortega-Liebana, J. Santamaria and S. B. Cronin, *Catal Commun*, 2014, **56**, 115-118.
24. L. Uson, M. G. Colmenares, J. L. Hueso, V. Sebastian, F. Balas, M. Arruebo and J. Santamaria, *Catal Today*, 2014, **227**, 179-186.
25. L. Uson, J. L. Hueso, V. Sebastian, S. Irusta, M. Arruebo, J. Santamaria, R. Arenal and I. Florea, *Catal Commun*, 2017, **100**, 93-97.
26. G. Hofmann, G. Tofighi, G. Rinke, S. Baier, A. Ewinger, A. Urban, A. Wenka, S. Heideker, A. Jahn, R. Dittmeyer and J. D. Grunwaldt, *Journal of Physics: Conference Series*, 2016, **712**, 012072.
27. A. M. Pérez-López, B. Rubio-Ruiz, V. Sebastián, L. Hamilton, C. Adam, T. L. Bray, S. Irusta, P. M. Brennan, G. C. Lloyd-Jones, D. Sieger, J. Santamaría and A. Unciti-Broceta, *Angew. Chem. Int. Ed.*, 2017, **56**, 12548-12552.
28. M. Signoretto, F. Menegazzo, A. Di Michele and E. Fioriniello, *Catalysts*, 2016, **6**.
29. L. Uson, V. Sebastian, A. Mayoral, J. L. Hueso, A. Eguizabal, M. Arruebo and J. Santamaria, *Nanoscale*, 2015, **7**, 10152-10161.
30. S. Marre and K. F. Jensen, *Chem Soc Rev*, 2010, **39**, 1183-1202.
31. P. M. Valencia, O. C. Farokhzad, R. Karnik and R. Langer, *Nature Nanotechnology*, 2012, **7**, 623-629.
32. L. Gomez, V. Sebastian, S. Irusta, A. Ibarra, M. Arruebo and J. Santamaria, *Lab Chip*, 2014, **14**, 325-332.
33. V. Sebastian, C. D. Smith and K. F. Jensen, *Nanoscale*, 2016, **8**, 7534-7543.
34. V. Sebastian and K. F. Jensen, *Nanoscale*, 2016, **8**, 15288-15295.
35. E. J. Roberts, S. E. Habas, L. Wang, D. A. Ruddy, E. A. White, F. G. Baddour, M. B. Griffin, J. A. Schaidle, N. Malmstadt and R. L. Brutchey, *Acs Sustain Chem Eng*, 2017, **5**, 632-639.
36. H. D. Jin, A. Garrison, T. Tseng, B. K. Paul and C. H. Chang, *Nanotechnology*, 2010, **21**.
37. C. H. Choi, E. Allan-Cole and C. H. Chang, *J Mater Chem C*, 2015, **3**, 7262-7266.
38. C. H. Choi and C. H. Chang, *Cryst Growth Des*, 2014, **14**, 4759-4767.
39. V. Sebastian, N. Zaborenko, L. Gu and K. F. Jensen, *Cryst Growth Des*, 2017, **17**, 2700-2710.
40. A. Schlange, A. R. dos Santos, U. Kunz and T. Turek, *Beilstein J Org Chem*, 2011, **7**, 1412-1420.
41. S. K. Lee, X. Y. Liu, V. S. Cabeza and K. F. Jensen, *Lab Chip*, 2012, **12**, 4080-4084.
42. Y. J. Song, J. Hormes and C. S. S. R. Kumar, *Small*, 2008, **4**, 698-711.
43. Z. X. Zhang, Z. Jiang and W. F. Shangguan, *Catal Today*, 2016, **264**, 270-278.
44. E. M. Johansson, M. A. Ballem, J. M. Cordoba and M. Oden, *Langmuir*, 2011, **27**, 4994-4999.
45. F. Balas, M. Manzano, M. Colilla and M. Vallet-Regí, *Acta Biomater.*, 2008, **4**, 514-522.
46. V. S. Cabeza, S. Kuhn, A. A. Kulkarni and K. F. Jensen, *Langmuir*, 2012, **28**, 7007-7013.
47. R. L. Hartman, J. P. McMullen and K. F. Jensen, *Angew Chem Int Edit*, 2011, **50**, 7502-7519.
48. J. Gu, Y. W. Zhang and F. Tao, *Chem Soc Rev*, 2012, **41**, 8050-8065.
49. C. J. Murphy and J. M. Buriak, *Chem Mater*, 2015, **27**, 4911-4913.
50. A. Y. Khan, S. B. Noronha and R. Bandyopadhyaya, *J Porous Mat*, 2015, **22**, 369-378.
51. M. D. Argyle and C. H. Bartholomew, *Catalysts*, 2015, **5**, 145-269.
52. J. J. Spivey, *Ind Eng Chem Res*, 1987, **26**, 2165-2180.
53. S. Todorova, A. Naydenov, H. Kolev, J. P. Holgado, G. Ivanov, G. Kadinov and A. Caballero, *Appl Catal A*, 2012, **413–414**, 43-51.
54. N. Navascués, M. Escuin, Y. Rodas, S. Irusta, R. Mallada and J. Santamaría, *Ind Eng Chem Res*, 2010, **49**, 6941-6947.